JOURNAL OF MATERIALS SCIENCE 29 (1994) 3281–3294

Scratching experiments on quartz crystals: orientation effects in chipping

C.R. TELLIER, D. BENMESSAOUDA
Laboratoire de Chronométrie, Electronique et Piézoélectricité, Ecole Nationale Supérieure de Mécanique et des Microtechniques, La Bouloie, Route de Gray, 25030 Besançon Cedex, France

The deformation and microfracture properties of quartz crystals were studied by scratching experiments. The critical load at which microfractures are initiated was found to be orientation dependent, whereas the average width of ductile grooves and chips remained relatively insensitive to crystal orientation. In contrast, a marked anisotropy in the shape of chips was observed. This anisotropy has been interpreted in terms of microfractures propagating preferentially along slip planes. Simple geometrical conditions for the SEM observation of active slip planes are proposed.

1. Introduction

The construction of quartz resonators requires thin quartz plates which are commonly processed by mechanical lapping and polishing [1–3]. However, surface damages such as microcracks induced by abrasion processes can markedly degrade the metrological performances of quartz resonators [1, 3–5]. An optimization of abrasion processes is then needed; such an optimization encompasses an understanding of conditions for the initiation and the subsequent propagation of microfractures.

Scratching experiments are finding increasing applications in the study of abrasive wear [6–9]. Elementary abrasive wear grooves are generally produced by indentors with simple shape [6, 7, 10–12] (spheres, cones and pyramids) which translate at a constant speed across the specimen surface. However, most of the experiments on brittle materials are devoted to the study of static indentation tests [13–17] made specially using Hertz's analysis [11, 13, 14, 16] which, for isotropic materials, predicts that microcracks nucleate at points of maximum tensile stress. This result is maintained for sliding spherical indentors, but sliding tangential force changes the stress trajectory pattern asymmetrically and causes a decrease in the critical normal load, P_C, for microcracking [10].

Moreover, in practice, the nucleation of a microcrack also depends on the initial surface damage [14, 17–19]. In particular, it has been found that inherent surface flaws can act as potential nuclei for crack growth in brittle solids. In addition, static hertzian tests made on anisotropic crystals have provided evidence both of a correlation between indentation shapes and the symmetry of the crystal [17, 19–21] and of a preferential propagation of fractures on cleavage planes (silicon crystal [20]) or on crystallographic slip planes of low index (quartz crystal [17, 19]).

Up to now, the number of static indentation tests performed on crystals has been limited. For quartz crystal, only Hartley and Wilshaw [17] have studied the deformation and fracture properties of three principal cuts of the quartz crystal in order to outline the role played by environmental parameters (moisture, temperature) in fracture nucleation. To our knowledge, no work has centred on the microcracking of various quartz surfaces under a sliding indentor. The purpose of this paper is to present results on the surface microcracking of differently oriented quartz surfaces. First, changes in the characteristic dimension of grooves (ductile formation of grooves) and in the shapes of microcracks with normal load and crystal orientation are systematically studied. Second, the action of slip planes in microcracking is investigated and emphasis is placed on the identification of slip planes which take an active part in propagation of fractures.

2. Experimental procedure

2.1. Materials

The quartz crystal belongs to the class 32. The slip planes are identified with reference to the crystal lattice (a_1, a_2, a_3, c) in Table I. They correspond respectively to the rhombohedral r faces and to the conventionally denoted Y and Z cuts [22]. Adopting the conventions specified by the IEEE standards on piezoelectricity the orientation in space (x, y, z) of a doubly-rotated plate is defined by means of a two angles of cut (φ, θ) (Fig. 1a). Fig. 1b shows that the prism and pyramid planes intersect the basal plane along three linear traces, respectively parallel to FH (planes P_1 and $\mathscr{P}_1$), EH (P_2 and $\mathscr{P}_2$) and EF (P_3 and $\mathscr{P}_3$).

Four differently-oriented plates (Table II) were cut in the same zone of a synthetic α-quartz crystal. The

0022–2461

TABLE I Identification of slip planes

Pyramidal planes	$(0\bar{1}11)$	$(\bar{1}101)$	$(10\bar{1}1)$
Prism planes	$(0\bar{1}10)$	$(\bar{1}100)$	$(10\bar{1}0)$
Basal plane	(0001)		

TABLE II The differently oriented quartz plates

Cut	Plane	Angle of cut	
		ϕ (deg)	θ (deg)
Z-cut	(0001)	0	90
X-cut	$(\bar{1}100)$	90	0
Y-cut	$(11\bar{2}0)$	0	0
AT-cut		0	35

orientations (ϕ, θ) were determined using a double X-ray goniometer which offers an accuracy of about 10 s. Before the tests were carried out, the quartz surfaces were mechanically polished and then carefully cleaned to remove contamination and abrasive particles. Each plate possesses a flat mark (Fig. 1C) to locate easily the direction of the X axis (Y, Z and AT cuts) or of the Y axis (X cut).

2.2. The scratching apparatus

The apparatus used in the tests was designed from a basic Leitz miniload 2 for Vickers hardness indentation tests. Scratches of total length $L_T = 3$ mm were made by moving the sample at a constant speed, V_T, under the vertically loaded Vickers indentor. The indentor is oriented as indicated in Fig. 2a. The normal load could be varied from 10–100 g so that one may reasonably expect to observe the transition ductile → brittle. The translation speed, V_T, could be chosen in the range [5–15 mm s^{-1}]. Tests are performed in air at room temperature; the temperature is controlled within $\pm$ 0.5 °C.

The tangential, lateral and normal forces (Fig. 2b) were measured using a piezoelectric three-dimensional sensor. The microcomputer-based apparatus allowed us to record the forces F_N and F_T at any length L of the run and to evaluate at L dimension parameters characteristic of a scratch (Section 3.3) because images of scratches made along various directions, D_Ψ, were simultaneously viewed on a 512 × 512 pixels display monitor. The angle ψ on Fig. 1c defines the direction of scratching.

2.3. Experimental parameters

Two parameters, namely the hardness (resistance to deformation), H_s, and the toughness (resistance to fracture), K_C, are widely used [15, 23] as convenient parameters to describe the two possible mechanical responses (i.e. deformation and fracture) of a surface material to a sliding indentor.

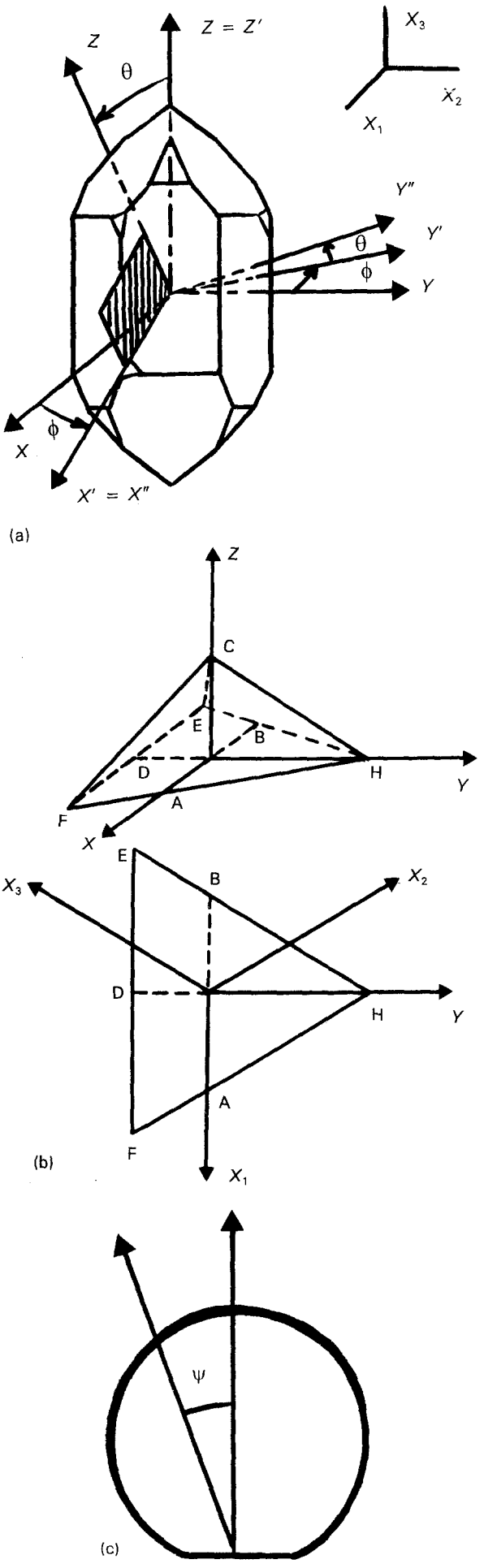

Figure 1 (a) Definition of the angles of cut, ϕ and θ. (b) The slip planes for the quartz crystal. (c) Definition of the angle Ψ for AT–Y– and Z– cut plates.

Experiments give the friction coefficient $f_A = F_T/F_N$, which governs the ductile → brittle transition [6, 7, 11, 12]. Thus, complementary measurements of the width, $2a$, of wear grooves are needed to evaluate the hardness (Fig. 2c)

$$H_s = \alpha_1 F_N/(2a)^2 \quad (1)$$

which characterizes the elastic deformation process in a wide range of solids provided the load, P, does not reach the critical load, P_C, at which microfractures are initiated. α_1 is a constant determined by indentor geometry. Let us recall that for loads exceeding the critical load the median crack length, c, is associated with the toughness by means of the relation [23]

$$K_C = \frac{F_N}{\beta_1 (2c)^{3/2}} \qquad c \gg a \quad (2)$$

where β_1 is an indentor constant. In practice, the path length of a median crack can only be estimated from images taken in transmitted light. The observation of cracks along the total length of run is then excluded. Therefore, in this study we overcame these difficulties by assuming that the length of lateral microcracks does not differ from that of median cracks as frequently observed for isotropic solids. When lateral cracks intersect the reference surface, chips of width c_s are formed (Fig. 2c). Because chips are directly accessible to vision it is possible to estimate c_s at any length run. In reality, the description of geometrical parameters $2a$ and $2c_s$ was achieved using a microcomputer and conventional numerical procedures for images analysis with a final program [24] furnishing statistical values $2a_{av}$ and $2c_{av}$ for these parameters.

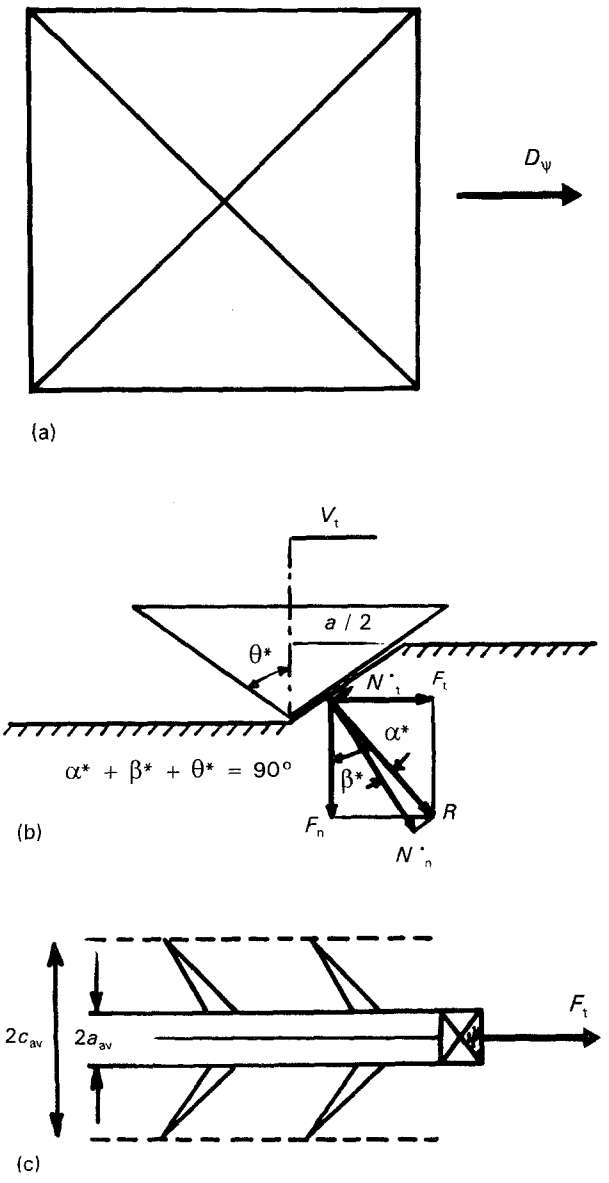

Figure 2 (a) Geometry of the indentor. (b) Definition of tangential, F_T, and normal, F_N forces. (c) Geometrical parameters $2a$ and $2c$.

3. Results

3.1. The deformation → chipping transition

It is expected that by increasing the normal load, P, from 5 g to 100 g, the critical load, P_C, at which microcracks are initiated may easily be determined. However, the introduction of sliding motion on a brittle surface significantly lowers the normal load required to produce micro-cracking. In some cases, scratching with a normal load as light as 5 g can induce surface microcracking in brittle solids [25]. Thus, for convenience we restrict our study to the observation by scanning electron microscopy (SEM) of microchipping along scratches. As a consequence, the critical load is identified with the limiting load, P^*, which causes surface chipping.

Scanning electron micrographs allows us to follow the changes in the deformation → chipping transition with orientation (ϕ, θ), of plates, with the direction, D_Ψ, of scratches and with the translation speed, V_T. Because the results are found to be independent of V_T, we only report here data obtained with a speed $V_T = 10\ \text{mm s}^{-1}$. Figs 3–7 illustrate some typical results. There are three particularly interesting features as revealed by these figures

1. At fixed angles (ϕ, θ) and fixed D_Ψ, scratches exhibit a quasi-ductile behaviour (Figs 3 and 4a–c, for example) as long as the load does not reach the threshold load, P^*. In this "ductile" region, the width, $2a$, of a scratch increases with load (see Fig. 3a–c, for example) as expected. Upon attaining P^*, chips begin to develop but "ductile" regions are still present along a run (see Figs 3d, 5c and 6c). With further increase in load, chips enlarge and the distance separating them decreases dramatically.

2. The threshold load, P^*, for a given plate depends on the direction of scratching (directional effect). The directional effects in P^* are completely revealed only by viewing scratches along the total run, L_T. Although the scanning electron micrographs displayed in Figs 3–6 illustrate partly the directional effects, let us, for example, turn our attention to Figs 5 and 6 relative to a Z-cut plate. These figures indicate without ambiguity that chips are formed for $P^* = 10$ g when D_Ψ coincides with the Y-axis, whereas such a load causes no chipping when the scratch is made along the X-axis. Moreover, the shape of chips produced for $P \gg P^*$ seems to be sensitive to the direction of scratching.

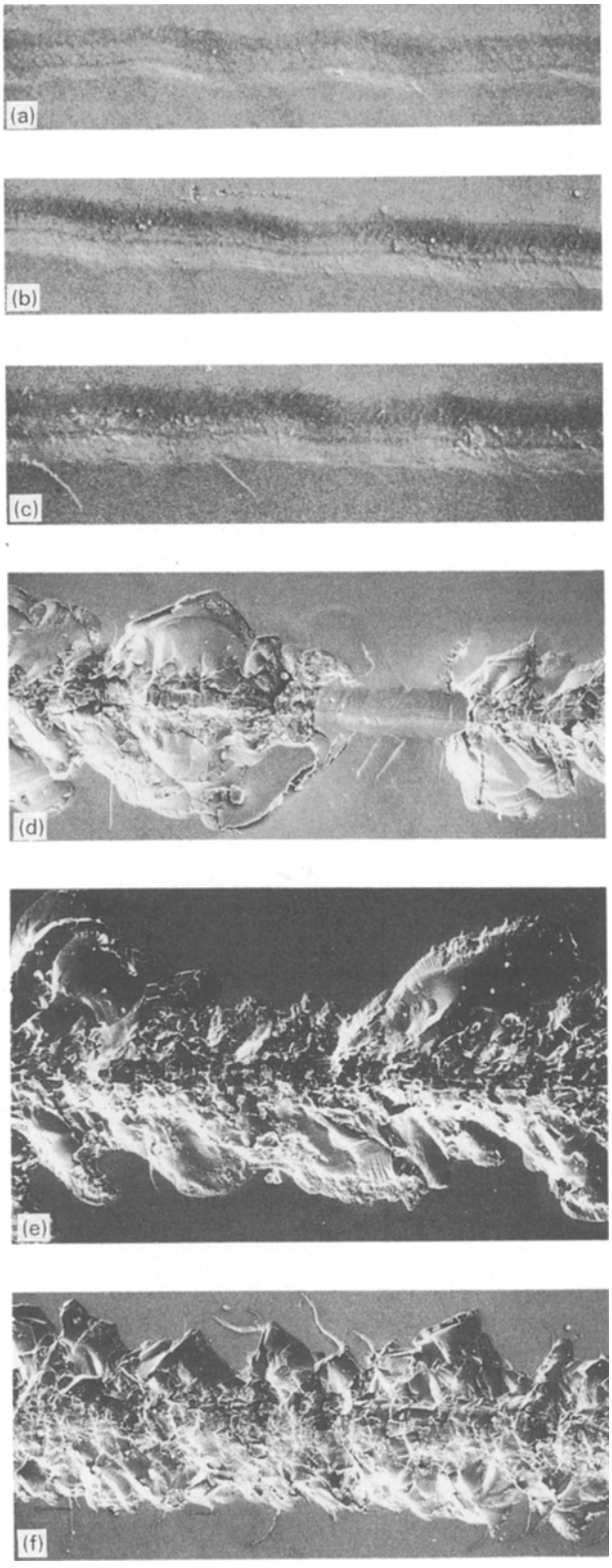

Figure 3 Changes with load, P, in scratches made along the Z direction on an Y-cut plate : (a–f) P = 5, 10, 15, 25, 50 and 100 g, respectively. (a) × 4000, (b, c) × 3000, (d, e) × 1500, (f) × 750.

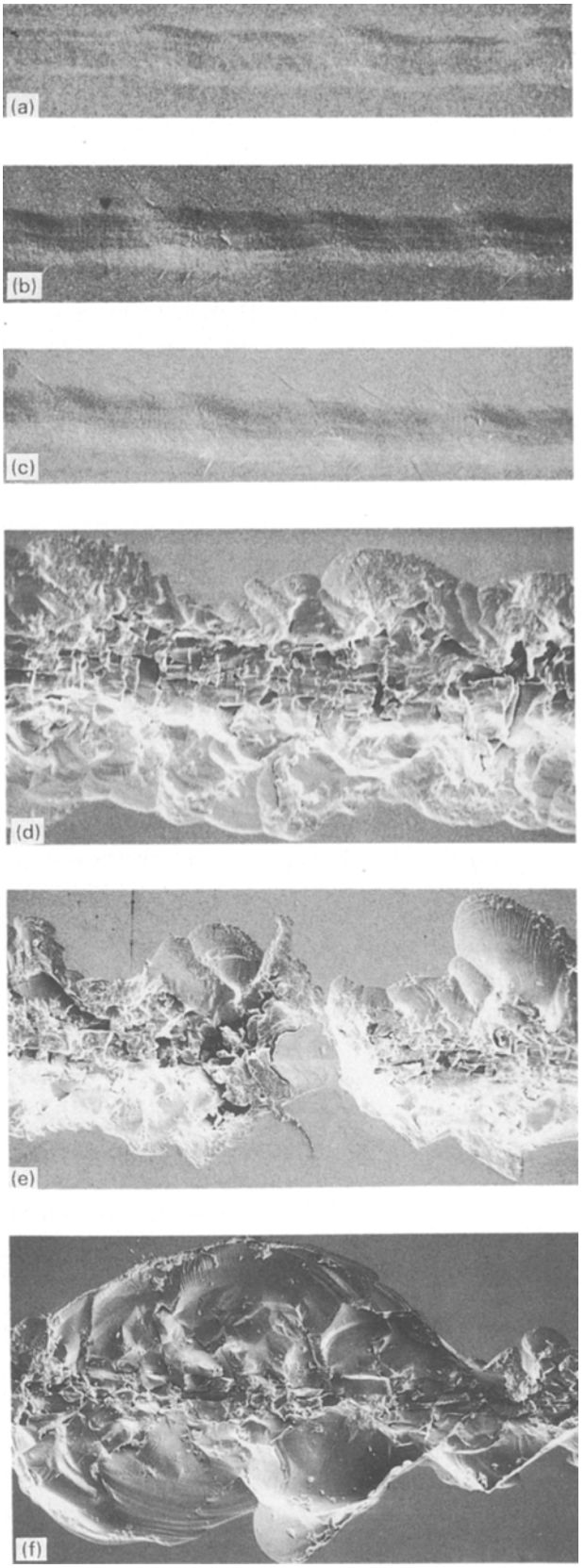

Figure 4 Changes with load, P, in scratches made along the Z-direction on an X-cut plate : (a–f), P = 5, 10, 15, 25, 50 and 100 g, respectively. (a) × 4000, (c) × 2700, (b, d) × 3000, (e) × 1500, (f) × 750.

3. For scratches carried out along a direction common to several differently oriented plates, the threshold load, P^*, is found to exhibit an orientation effect. Let us examine, for example, the scanning electron micrographs presented in Figs 6 and 7 relative to X-scratches made, respectively, on Z- and AT-cut plates: one can depict orientation effects which clearly not only concern the threshold load but also the extent and the shape of chips. This last point will be discussed later.

Threshold values for the normal load (Table III) were estimated from a complete analysis of scratch

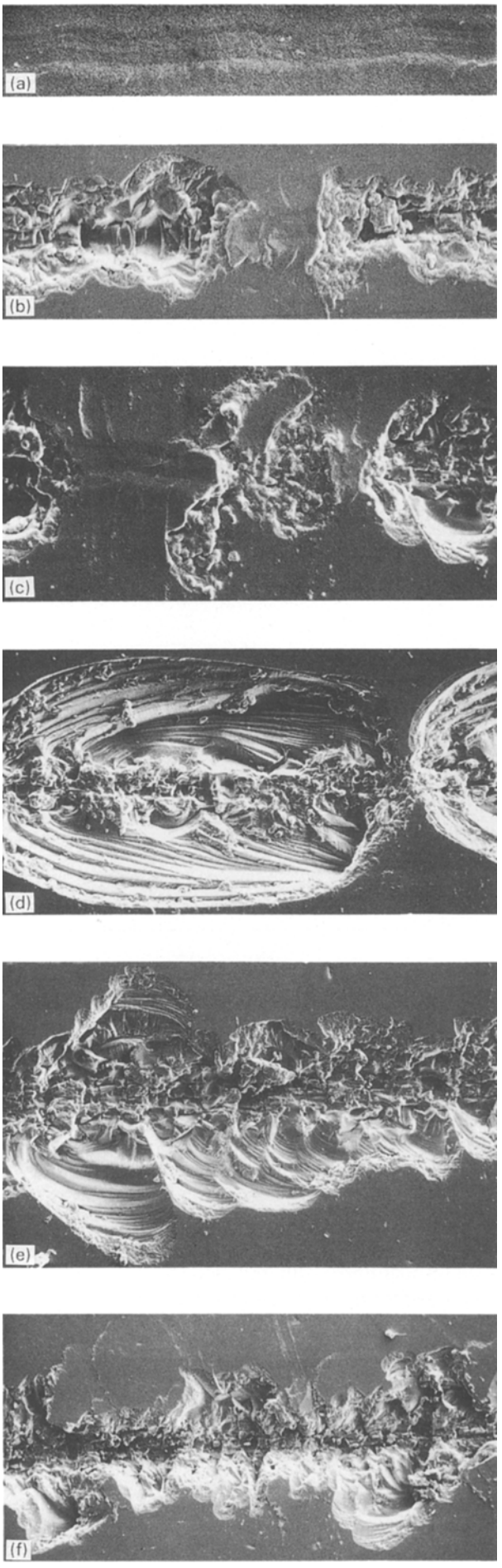

Figure 5 Changes with load, P, in scratches made along the Y-direction on an Z-cut plate: (a–f) P = 5, 10, 15, 25, 50 and 100 g, respectively. (a) × 4000, (b, c) × 3000, (d, e) × 1500, (f) × 750.

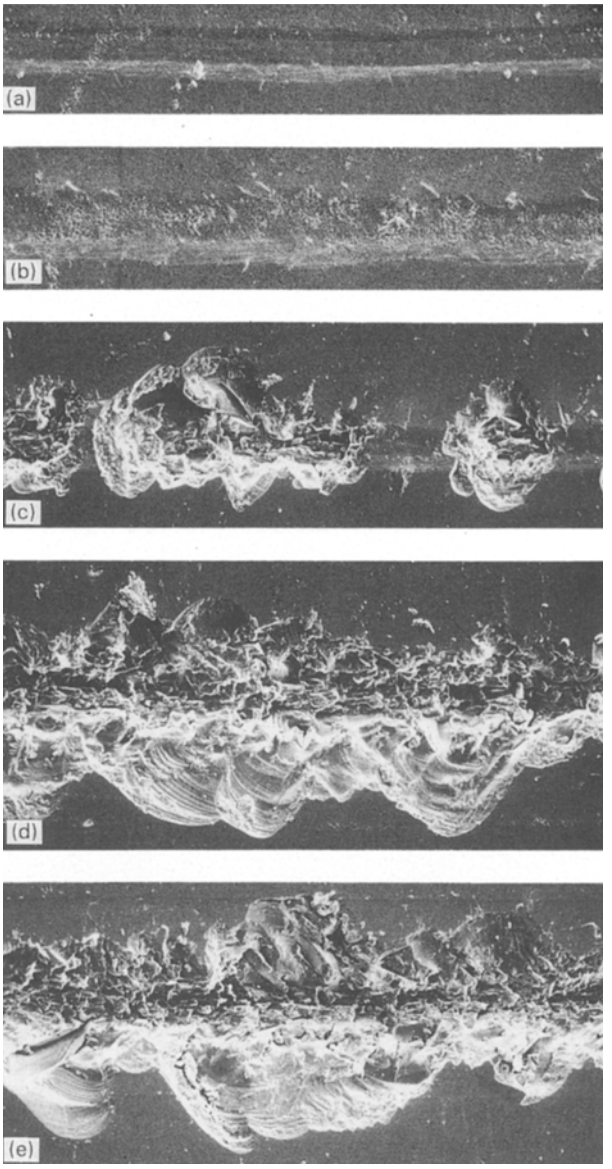

Figure 6 Changes with load, P, in scratches made along the X-direction on a Z-cut plate: (a–f) P = 10, 15, 25, 50 and 100 g, respectively. (a, b) × 3000, (c, d) × 1500, (e) × 750.

views. Clearly the load at which chipping occurs is determined principally by the crystal orientation. Such an assumption agrees with previously published results relative to indentation tests [17].

3.2. The average geometrical parameters $2a_{av}$ and $2c_{av}$

The geometrical parameters $2a$ and $2c_s$, as viewed on the monitor screen, were averaged over the total length, L_T, of scratches made along various directions, D_Ψ. For "heavy" loads (typically $P > 25$ g), "ductile" region can be recognized along the tracks, and then only the average value $2c_{av}$ emerges from numerical calculations.

Figs 8–11 show the experimental variations in the averaged dimension parameters $2a_{av}$ and $2c_{av}$, with the normal load, P, for five different scratching tests made on various quartz plates. Generally, for a given cut, the average parameters remain quasi-independent of the direction D_Ψ. Only the Y-cut plate departs from

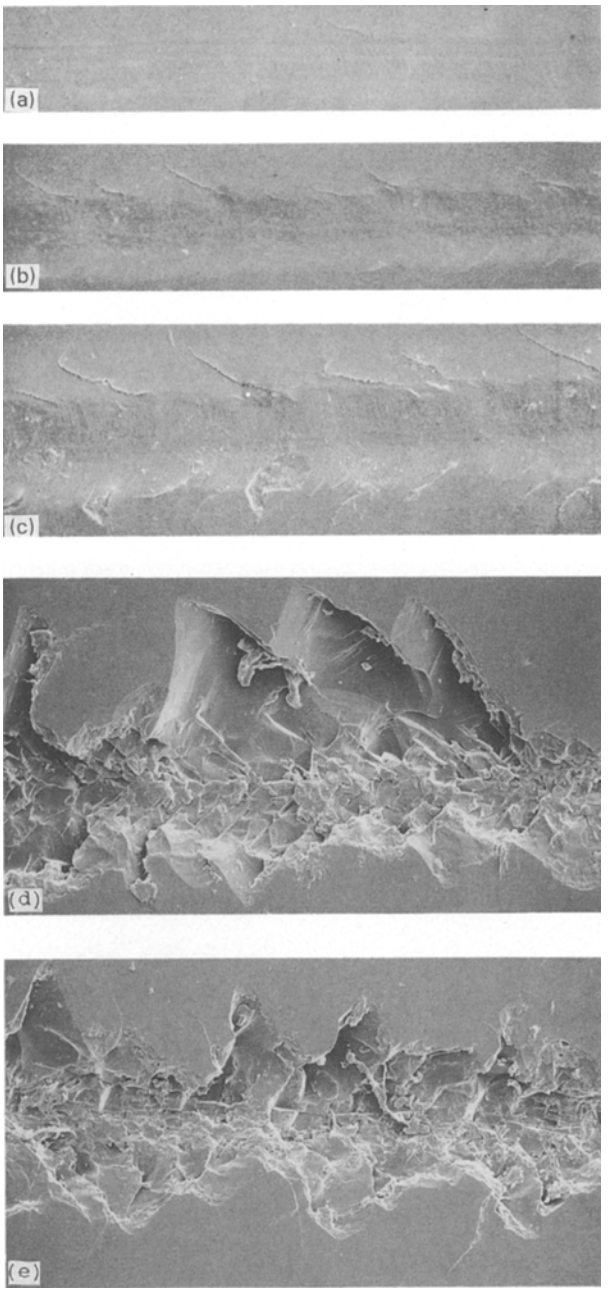

Figure 7 Changes with load, P, in scratches made along the Y-direction on an AT-cut plate: (a–e) $P = 5$, 15, 25, 50 and 100 g, respectively. (a) × 4000, (b, c) × 3000, (d) × 1000, (e) × 750.

this behaviour: the geometrical parameters $2a_{av}$ and $2c_{av}$ exhibit effectively slight directional effects and the data are fitted to two distinct curves with respect to the scratching direction. In Fig. 9 we observe that the deviation between the two curves never exceed 25% for $2c_{av}$ and 15% for $2a_{av}$, thus the observed directional effects are not very significant. For all the other cuts studied here, the average parameters, $2a_{av}$ and $2c_{av}$, remain virtually unaltered with changes in direction, D_Ψ. Under these conditions the variations in geometrical parameter ($2a_{av}$ and $2c_{av}$) with load can be conveniently fitted by means of an average plot ($2a^*$ versus P or $2c^*$ versus P plot) as typified by curves in Figs 8–11.

At this point, it should be noted that the average value, $2a_{av}$, of the width of "ductile" grooves differs from the true value $2a_{true}$ as evaluated from the scanning electron micrographs. This deviation may be attributed to humped edges produced by scratching which cannot be easily distinguished for a transparent material. In practice, these two lateral boundaries are visually identified with the bottom of grooves and accounted for in the numerical evaluation of the average width, $2a_{av}$, of "ductile" grooves.

Each of the $2a^*$ and $2c^*$ versus P plots, as drawn in Figs 8–11 shows a steady increase in the geometrical parameter with load followed by a quasi-saturating behaviour in the heavy load region ($P > P^*$). Taking this observation, into account, attempts are made to obtain useful information about the nature of the dependence of geometrical parameter on the normal load by plotting $\ln 2a^*$, $\ln 2a_{true}$ and $\ln 2c^*$ against $\ln P$ (Figs 12 and 13). In all cases, changes in the geometrical parameters with load give straight lines. Thus, the effect of loading on the geometrical parameters is accurately represented by simple equations of the

TABLE III The threshold load, P^*, for differently oriented quartz plates

Cut	Angle, ψ (deg)	Load, P^* (g)
Z-cut	0	15
	90	10
X-cut	0	15
	90	15
Y-cut	0	25
	90	15
AT-cut	0	25
	90	10

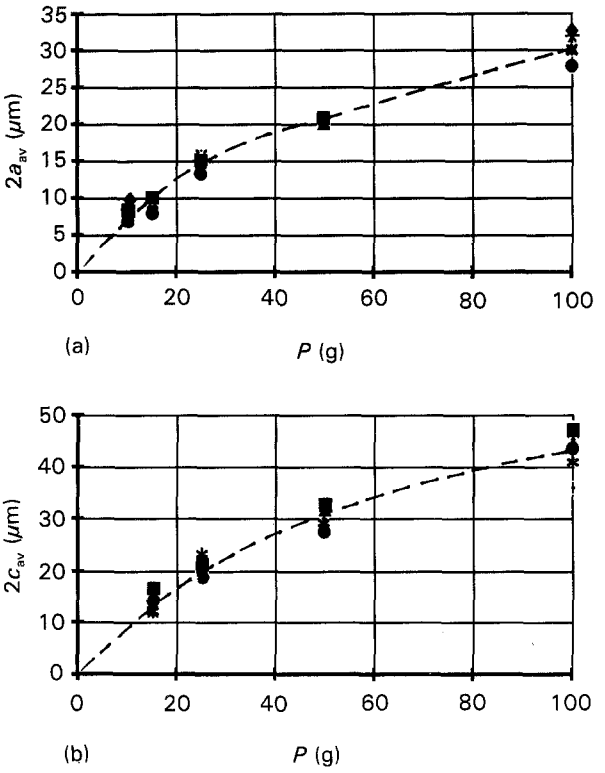

Figure 8 Variations of the geometrical parameters (a) $2a_v$ and (b) $2c_v$ with normal load P for various sliding directions. D_Ψ. Ψ: (●) 90°, (■) 45°, (◆) 30°, (▲) 15°, (*) 0°, X-cut plate.

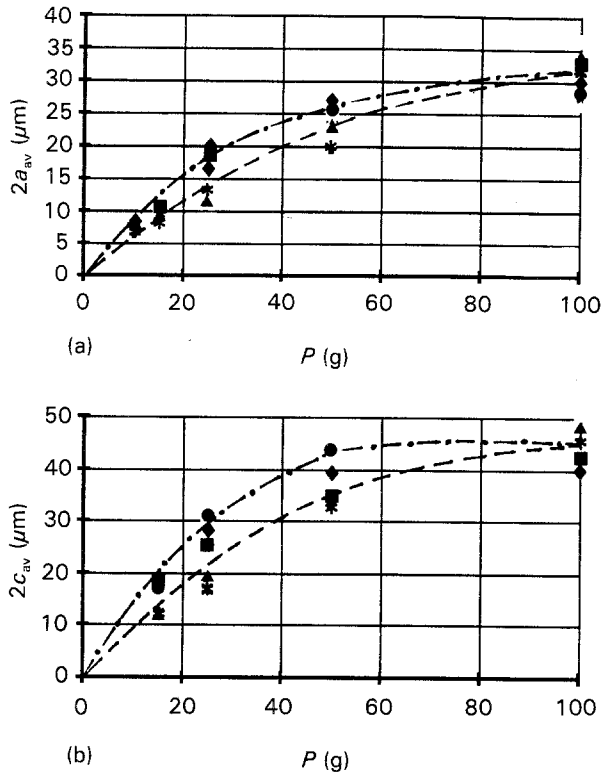

Figure 9 Variations of the geometrical parameters (a) $2a_v$ and (b) $2c_v$ with normal load, P, for various sliding directions, D_Ψ. Ψ: (●) 90°, (■) 45°, (◆) 30°, (▲) 15°, (∗) 0°. Y-cut plate.

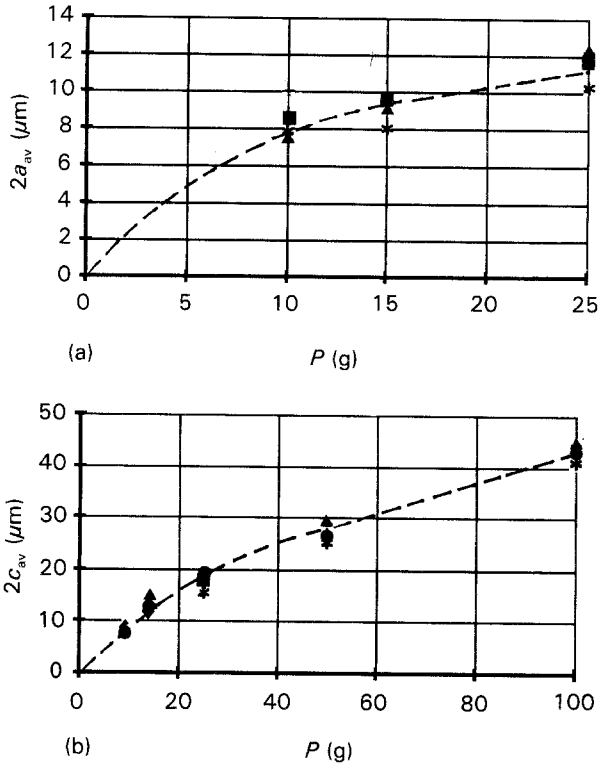

Figure 10 Variations of the geometrical parameters (a) $2a_v$ and (b) $2c_v$ with normal load, P, for various sliding directions, D_Ψ. Ψ: (●) 90°, (■) 45°, (◆) 30°, (▲) 15°, (∗) 0°. Z-cut plate.

form

$$2a^* = b_{a^*} P^{m_{a^*}} \quad (3)$$

$$2c^* = b_{c^*} P^{m_{c^*}} \quad (4)$$

where b_{a^*}, b_{c^*}, m_{a^*} and m_{c^*} can act as orientation-dependent constants. The parameter $2a_{true}$ exhibits a quite similar behaviour and from Figs 12 and 13 it can be seen that the simple relations

$$m_{a_{true}} = m_{a^*} \quad (5)$$

$$2a^* \approx 2a_{true} \quad (6)$$

hold for the various cuts under consideration.

Experimental values for the constant m_{a^*} (or m_{c^*}) and b_{a^*} (or b_{c^*}) can be respectively determined from the slope and the ordinate intercept of the $\ln 2a^*$ (or $\ln 2c^*$) versus $\ln P$ curve from Table IV which summarizes the main results. We can collate two interesting points:

(i) for the various cuts studied here, the constants m_{a^*} and m_{c^*} take nearly similar values. Then, on the one hand, differences in the mechanical response of the material (ductile deformation or fracture) do not modify the value for the exposant which, on the other hand, remains unaffected by the angles of cut. We then infer that the constant m characterizes the material only;

(ii) orientation effects are clearly depicted in the constants b_{a^*} and b_{c^*}. The constant b_{a^*} is weakly dependent on the orientation, whereas the constant b_{c^*} is a more rapidly varying function of the angles of cut. These more marked orientation effects in b_{c^*} can be interpreted in terms of differences in the shape of chips formed on differently oriented plates.

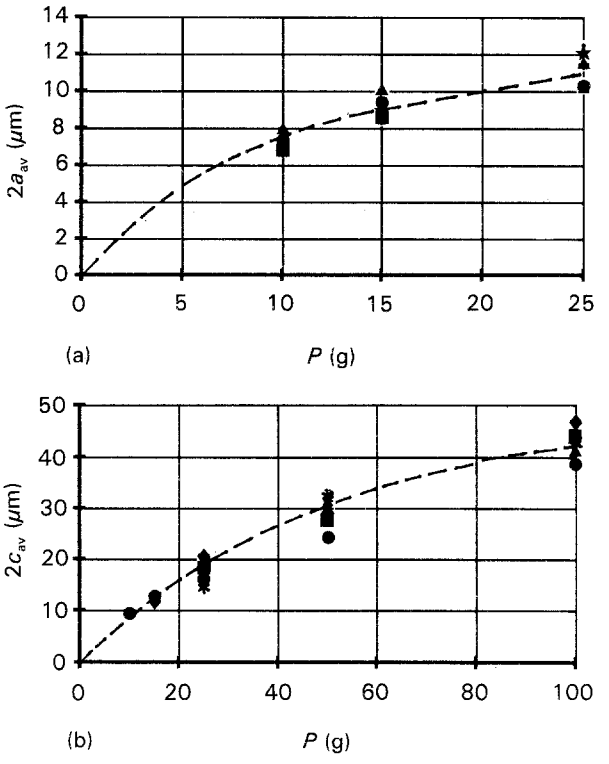

Figure 11 Variations of the geometrical parameters (a) $2a_v$ and (b) $2c_v$ with normal load, P, for various sliding directions, D_Ψ. Ψ: (●) 90°, (■) 45°, (◆) 30°, (▲) 15°, (∗) 0°. AT-cut plate.

3.3. Chipping and orientation

Careful examination of Figs 8–11 reveals an apparent dependence of the surface chipping on orientation and

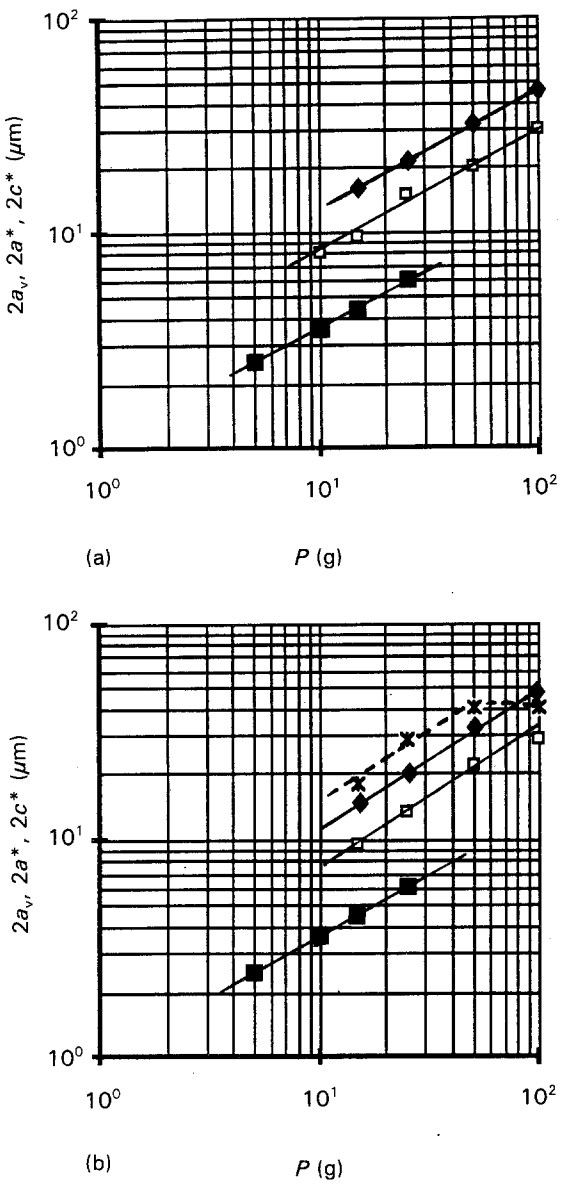

Figure 12 Plots of (□) ln $2a^*$, (■) ln $2a_{true}$ and (◆, ✳) ln $2c^*$ against ln$P$ for (a) X-cut plate, and (b) Y-cut plate.

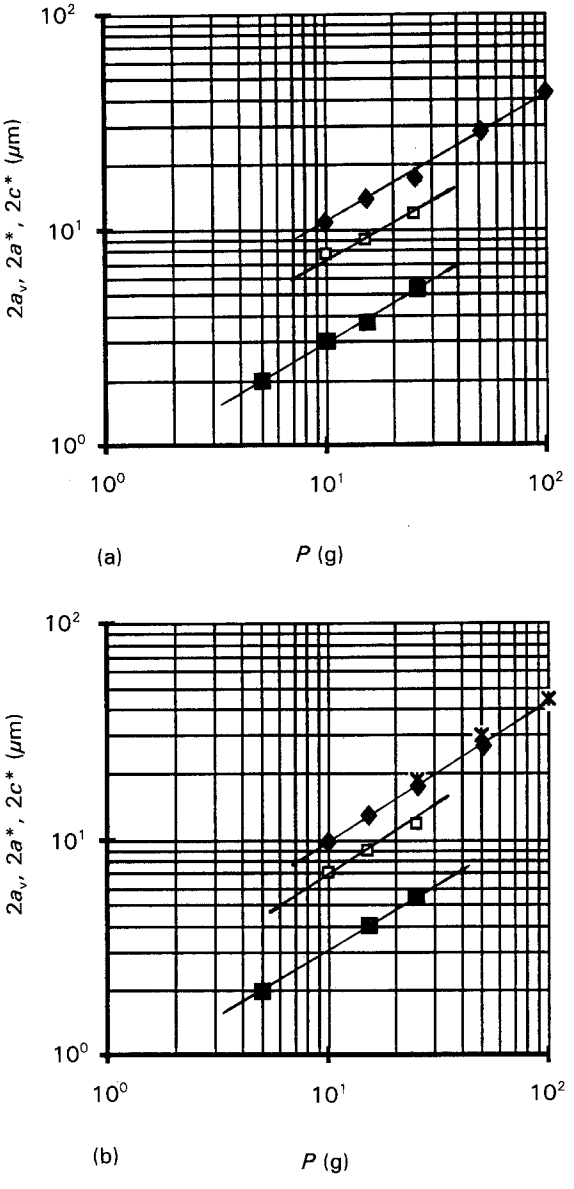

Figure 13 Plots of (□) ln $2a^*$, (■) ln $2a_{true}$ and (◆) ln $2c^*$ against ln$P$ for (a) Z-cut plate and (b) AT-cut plate.

TABLE IV Experimental values for the constants (b_{a*}, m_{a*}), (b_{c*}, m_{c*}) and (b_{at}, m_{at}) as evaluated from Figs 12 and 13. The subscript indicates a_{true}

	X-cut	Y-cut		Z-cut	AT-cut
		$\psi = 0°, 15°, 90°$	$\psi = 30°, 45°$		
b_{a*}, m_{a*}	2.1; 0.57	2.1; 0.57	– –	– –	– –
b_{at}, m_{at}	1; 0.57	1; 0.55	– –	0.74; 0.62	0.74; 0.63
b_{c*}, m_{c*}	5.2; 0.57	2.8; 0.62	3.8 0.59	2.5; 0.61	2.5; 0.62

on the direction of scratch with a lateral dimension, $2c$, very sensitive to angles (ϕ, θ) and to direction, D_Ψ. Therefore, we must now investigate more precisely the influence of angles (ϕ, θ) and of D_Ψ on the surface chipping. This is most conveniently achieved from the SEM observations relative to a normal load $P = 100$ g. Qualitative information can be extracted by examining the scanning electron micrographs displayed in Figs 14–17. To detect eventual directional effects, is obvious that for a given plate the shape of chips is governed by the direction D_Ψ. In particular, experiments on an X-cut plate give rise to partially formed chips (Fig. 14a–d), or to large chips with curved edges (Fig. 14e) when ψ passes, respectively, through 0° or 90°. Evidently, for a common fixed direction, D_Ψ, scratching on various plates causes the

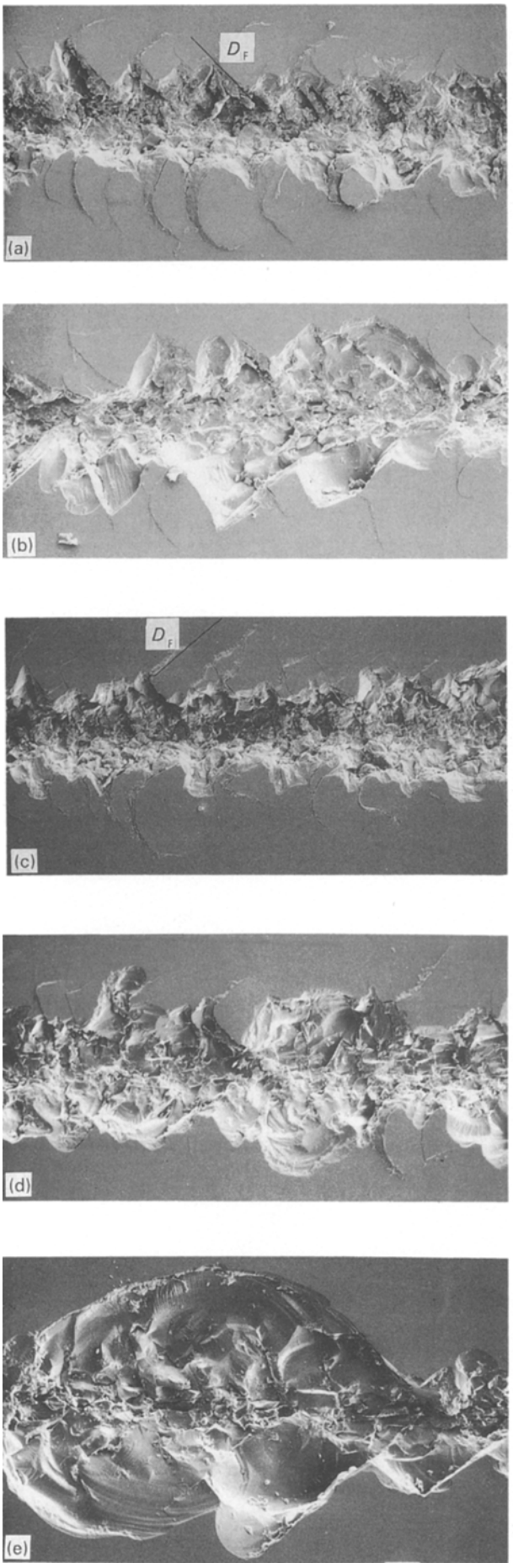

Figure 14 Evolution of the shape of chips with the sliding direction, D_Ψ for an X-cut plate. Ψ: (a) 0° (*Y*-axis), (b) 15°, (c) 30°, (d) 45°, (e) 90° (*Z*-axis). Some slip traces are indicated in the micrographs. ×750

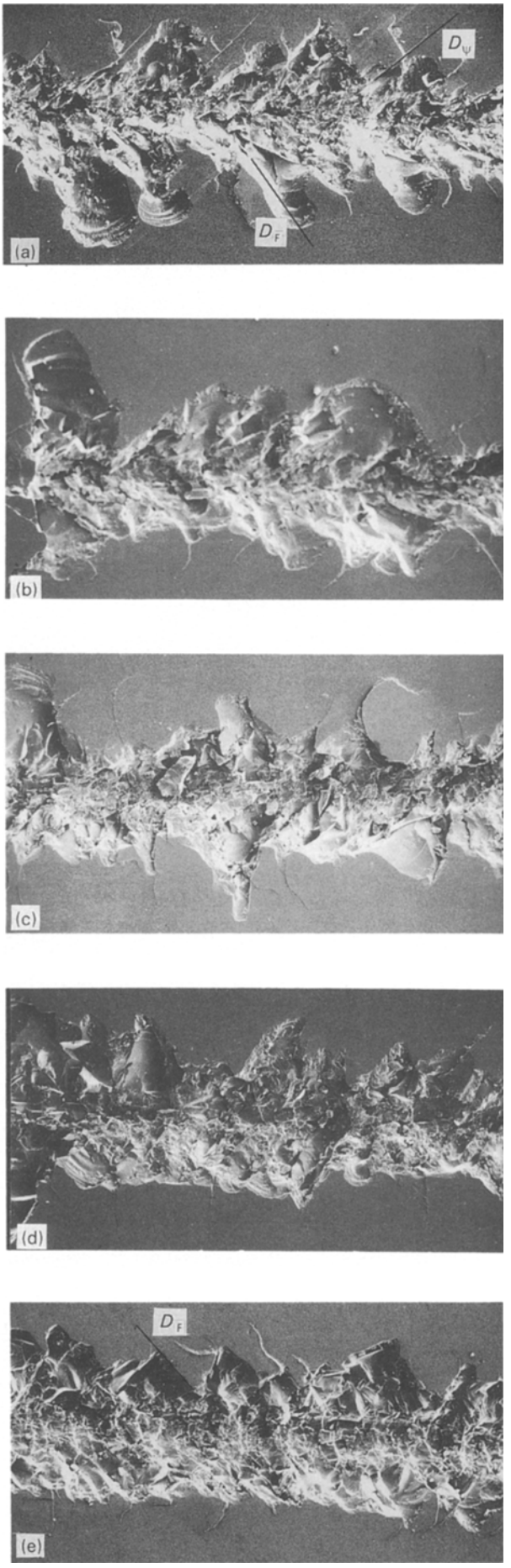

Figure 15 Evolution of the shape of chips with the sliding direction, D_Ψ for an Y-cut plate. Ψ: (a) 0° (*X*-axis), (b) 15°, (c) 30°, (d) 45°, (e) 90° (*Z*-axis). Some slip traces are indicated in the micrographs. ×750

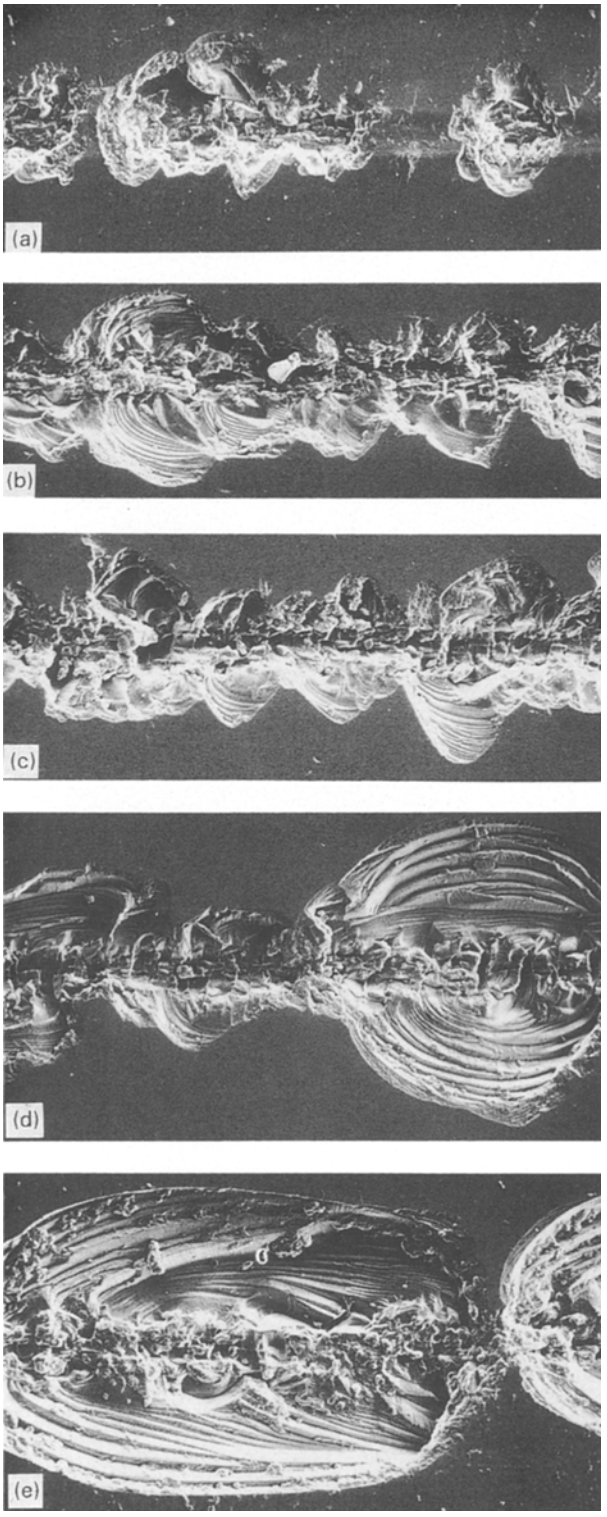

Figure 16 Evolution of the shape of chips with the sliding direction, D_Ψ, for a Z-cut plate. Ψ: (a) 0° (*X*-axis), (b) 15°, (c) 30°, (d) 45°, (e) 90° (*Y*-axis). Some slip traces are indicated in the micrographs. ×1500.

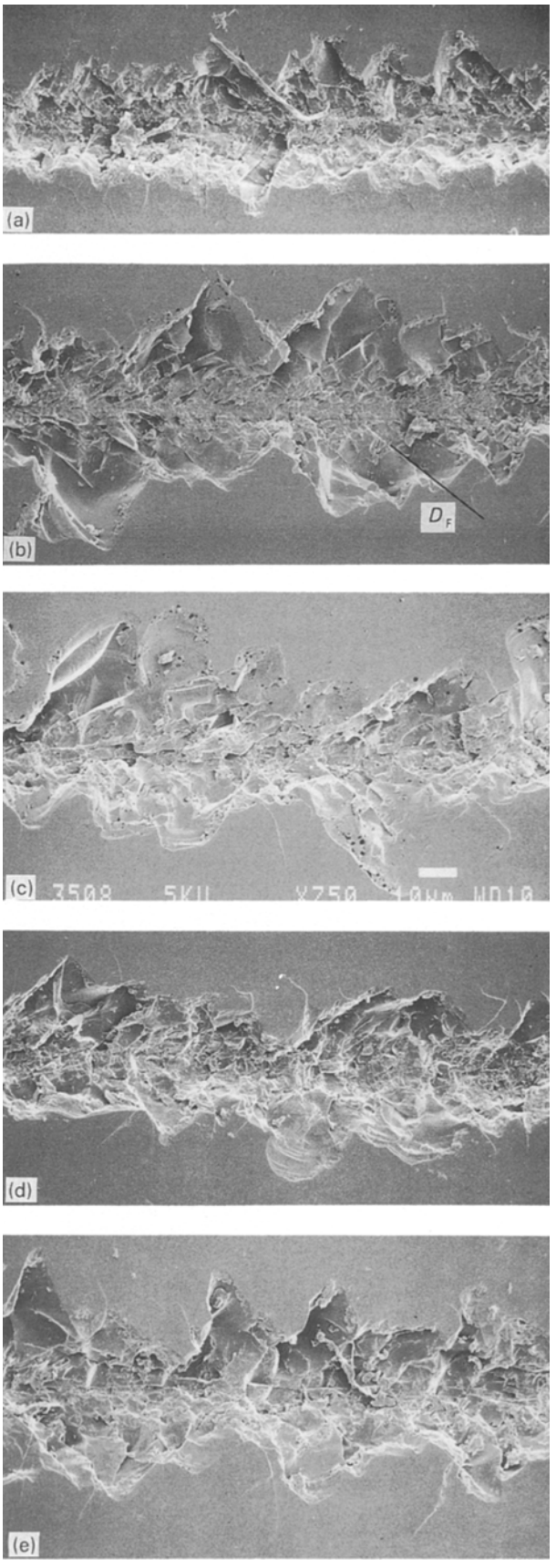

Figure 17 Evolution of the shape of chips with the sliding direction, D_Ψ for an AT-cut plate. Ψ: (a) 0° (*X*-axis), (b) 15°, (c) 30°, (d) 45°, (e) 90° (*Z'*-axis). Some slip traces are indicated in the micrographs. ×750.

development of differently shaped chips: it is sufficient, for example, to compare Fig. 14a with Fig. 16a or Fig. 14e with Fig. 15e.

4. Discussion

4.1. Anisotropic elastic properties of the quartz crystal

Let us recall that the averaged experimental values for constants b_{a^*} and b_{c^*} may take into account possible directional effects. In particular, the moderate deviations in the geometrical parameters caused by modifications in the sliding direction (Figs 8–11) can be understood in terms of slight directional effects. But

turning our attention to Section 3.3, it appears that the geometrical parameter $2c^*$ also exhibit some orientation effects. We can attempt to explain these orientation and directional effects in terms of the anisotropic elastic properties of quartz crystal [26].

For an isotropic material and a spherical indentor [10], the maximum tensile stress, σ_m, in the specimen is given by

$$\sigma_m = (1 + Bf)\left(\tfrac{1}{2} - \nu\right) P_0 \quad (7)$$

where P_0 is the averaged load, f the coefficient of kinetic friction, and B is a parameter related to Poisson's ratio, ν, of the isotropic material [10]

$$B = \frac{3\pi\ (4 + \nu)}{8\ (1 - 2\nu)} \quad (8)$$

In an anisotropic material, Poisson's ratio depends on orientation (ϕ, θ) and direction D_ψ. Then, as suggested by Hartley and Wilshaw [17], we must now take into account the angular variation of ν, (ϕ, θ, ψ).

In the present study, we are also concerned with a sharp indentor, and Equations 7 and 8 no longer hold. Then, for simplicity, we assume that the constant B remains insensitive to the angles of cut and to D_ψ. To estimate crudely the role played by the anisotropic elastic properties of the quartz crystal, we can now write simply

$$\nu(\phi, \theta, \psi) \approx \frac{S_{ij}}{S_{ii}} \quad (9)$$

where the S_{ij} are the compliance coefficients. The subscript j refers to the direction of normal loading and the subscript i corresponds to the direction of lateral strain.

Applying the approximate Equation 9 to the three principal cuts gives the results shown in Table V. We observe that the anisotropy due to the angular variation of the Poisson's ratio induces only slight changes in the maximum tensile stress (deviation less than 10%). The calculated deviation is of the same order of magnitude as the experimental deviation which, for the geometrical parameters, does not exceed 10%.

4.2. Symmetry of the crystal and planes of "easy cleavage"

Some authors [10, 17, 20, 21, 25] have argued that the symmetry of the crystal governs the shape of indentations produced by hertzian tests. Experimental studies of the hertzian fracture geometry of differently oriented surfaces of silicon [13, 20, 21] or of quartz [17] have provided evidence for symmetry exerting an influence on crack geometry. Moreover, several authors [17, 20] have pointed out that in anisotropic crystals, microcracks propagate preferentially along planes of easy cleavage, i.e. for the quartz crystal along slip planes.

If we take this explanation into consideration, it is obvious that fractures are formed along directions D_F characteristic of the angles of cut (ϕ, θ) and of the sliding direction, D_ψ. Figs 14–17 reveal clearly that the edges of chips are effectively aligned along preferential directions. Starting from this observation we assume that the chipping is essentially governed by the crystallographic slip planes with a low index (see Section 2.1.). A slip plane inclined with respect to the reference surface by an angle Δ (Fig. 18a) intersects this reference surface of orientation (ϕ, θ) in a straight line called, for convenience, the "slip trace". The direction of a slip trace with respect to the sliding direction is defined by means of the angle δ (Fig. 18b). For a given slip plane, it is evident that the angle Δ is determined only by the angles of cut.

As a first step, values for the angles Δ and δ are calculated for different cuts and for five directions of sliding (Table VI). In a second step, preferential directions D_F are recognized in Figs 14–17. We have, for

TABLE V Values of $\nu(\phi, \theta, \psi)$ as evaluated from Equation 9 for stresses measured along various directions D_ψ

Cut	$\nu(\phi, \theta, \psi)$	
	$\psi = 0°$:	$\psi = 90°$:
X-cut	0.134	0.094
Y-cut	0.134	0.094
Z-cut	0.125	0.125

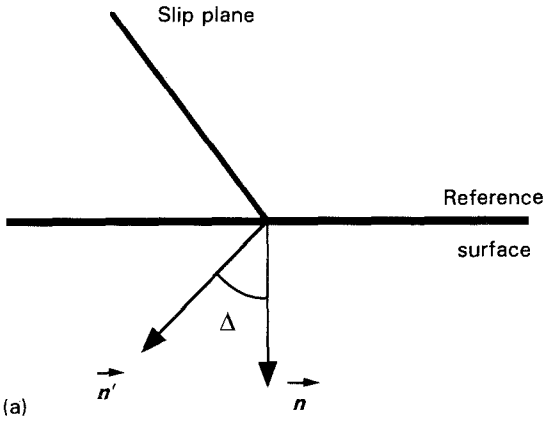

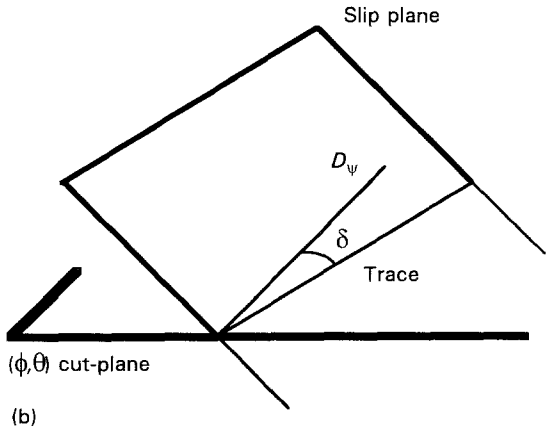

Figure 18 Definition of the angles (a) Δ and (b) δ.

TABLE VI Absolute values of angles δ and Δ for the X-, Y- and AT-cut plates and for various sliding directions, D_ψ

Cut	Slip plane	|δ| (deg) ψ: 0°	15°	30°	45°	90°	|Δ| (deg) ψ = 0°, 15°, 30° 45°, 90°
X-cut	P_1, P_2	32	47	62	77	58	47
	P_3	52	37	22	7	38	90
	p_1, p_2, p_3	90	75	60	45	0	30
	basal	0	15	30	45	90	90
Y-cut	P_1	48	63	78	93	42	67
	P_2	48	33	18	3	42	67
	P_3	0	15	30	45	90	38
	p_1, p_2, p_3	90	75	60	45	0	60, 60, 0
	basal	0	15	30	45	90	90
AT-cut	P_1	68	53	38	23	22	47
	P_2	68	83	82	67	22	47
	P_3	0	15	30	45	90	73
	p_1	68	53	38	23	22	66
	p_2	68	83	82	67	22	66
	p_3	0	15	30	45	90	35
	basal	0	15	30	45	90	55

convenience, distinguished between three types of cracks or fractures: (1) microcracks (f) aligned along a specified direction, (2) aligned fracture (f) at the bottom of chips, (3) chips (C) aligned parallel to the trace of a slip plane. Then the direction of alignment of microcracks, fractures and chips are identified when possible with a "slip trace". Tables VII–IX indicate, for different cuts and for various directions D_ψ, the slip planes which are found to participate in microcracking or chipping. Examination of these tables reveals that the prism planes are operative only for angles ψ in the vicinity of 30°, whereas pyramidal planes are involved in fracture and chipping mechanisms whatever the sliding direction. Moreover, we note that depending on D_ψ, all the slip planes are found to contribute actively to chipping.

Therefore, it may be of interest to correlate the possible contribution of a given slip plane to a favourable geometrical orientation of this slip plane with regard to the reference surface and to D_ψ. To decide if a slip plane plays a role in chipping we retain two simple conditions, connected to the values of the angles Δ and δ.

1. We must separate clearly the direction of alignment of a fracture or of a slip from the direction D_ψ of the groove. Then, we suppose that we can only identify fractures corresponding to relatively large |δ|. In practice, the identification is limited to fractures whose direction of alignment makes an angle $|\delta| > 30°$ with the direction D_ψ.

2. To explain the mechanism of chipping, we follow the description scheme adopted by Lawn and Swain [20]: median vents form during loading and lateral vents during unloading. If vents intersect a slip plane, they initiate chipping along this plane. Depending on the inclination, Δ, of the slip plane, fractures and chips with sharp edges can be formed. Such fractures and edges can be easily tracked on the scanning electron micrographs of sliding traces. The additional condition for an easy identification of fracture can now be written as $\Delta > 45°$.

TABLE VII Correlation between slip planes and the geometrical features of chips which are formed on an X-cut plate. Underlined features or planes correspond to: =, $|\Delta| \geq 60°$; – – –, $|\Delta| > 45°$; ——, $|\delta| > 30°$

ψ (deg)	P_1, P_2	P_3	p_1, p_2, p_3	Basal
0	f + F + C	f + F		
15	f + F + C	f + F + C	C	
30	f + F + C	f*	$F + f_R$	f*
45	f		$F + f_R + C$	F*
90				
Load: 100 g	F + C	F + C		

In Tables VII–IX, we have outlined the microcracks (f), fractures (F) and chips (C) which satisfy Condition 1, as well as the slip planes whose inclinations verify Condition 2. Several interesting features emerge from these tables, one may reasonably presume to reflect the role played by slip planes in chipping:

(i) all the slip planes seem to participate in fracture and chipping, but for a given cut and for a fixed D_ψ, we are able to recognize the contribution of a limited number of slip planes with $\Delta \geq 45°$ and for which $|\delta| > 30°$;

(ii) for the Z-cut plane, all the slip planes contribute to the development of large chips whose bottoms are covered by ridges associated with the fact that the Z-cut plane lies parallel to the basal plane and that the inclination, Δ, of prism and pyramidal planes with respect to the basal plane is 60° and 52°, respectively. Then we can assume that lateral vents develop parallel to the surface specimen and meet both pyramidal and prism planes. They then propagate along these slip planes before emerging at the specimen surface.

5. Conclusion

The results presented here on scratching of differently oriented quartz plates have provided evidence for both directional and orientation effects. These effects

TABLE VIII Correlation between slip planes and the geometrical features of ships formed on an Y-cut plate. Underlined features or planes correspond to : =, $|\Delta| \geq 60°$;——, $|\delta| > 30°$

ψ (deg)	$\underline{\underline{P_1}}$	$\underline{\underline{P_2}}$	P_3	$\underline{\underline{p_1}}$, $\underline{\underline{p_2}}$, p_3	Basal
0	f + F + C	f + F + C			
15	F + A	C	F*	f_R	F*
30	C		f*	F + C	f*
45	C		C + F	f + F + C	C + F
90					
Load: 100 g	f + F + C	f + F + C			f

TABLE IX Correlation between slip planes and the geometrical features of ships formed on an AT-cut plate. Underlined features or planes correspond to: =, $|\Delta| \geq 60°$;– –, $|\Delta| > 45°$;——, $|\delta| > 30°$

ψ (deg)	$\underline{P_1}$	$\underline{P_2}$	$\underline{\underline{P_3}}$	$\underline{\underline{p_1}}$	$\underline{\underline{p_2}}$	p_3	Basal
0	F + C	F + C					
15	F + C	f		f	C + F		
30		C	f + F + C	C		f + F + C	
45		C + F	C + F	C + F		F + C	C + F
90							
Load: 100 g	C*		C		C*	C	C

TABLE X Identification of various plates and different sliding directions of the slip planes which contribute to chipping

Cut	ψ (deg) 0	15	30	45	90
X-cut	(P_1, P_2), P_3	(P_1, P_2); P_3	(P_1, P_2), p_3	p_3	(P_1, P_2), p_3
Y-cut	P_1, P_2	P_1, P_2, p_2	P_1, p_2	P_1, P_3, p_2, basal	P_1, P_2, basal
Z-cut	Both prisms planes, pyramidal planes and the basal plane contribute to chipping				
AT-cut	P_1, P_2, p_1, p_2	p_1, p_2	P_2, p_1, P_3, p_3 basal	P_2, p_1, P_3, p_3 basal	P_3, p_3, basal

affect the critical load at which microfractures are initiated. However, in the ductile region, no marked changes in the width of grooves with the orientation of plates or with the direction of sliding, D_ψ, have been detected.

Changes in the angles of cut as well as in the direction D_ψ induce marked modifications in the shape of chips or in the extent of chipping along scratches. In contrast, the average width, $2c^*$, of chips remains quasi-unaffected. Moreover, the variations in the averaged geometrical parameters $2a^*$ and $2c^*$ with normal load P are found to follow the same simple type of laws.

The orientation effects cannot be explained solely in terms of the anisotropic elastic properties of quartz crystal. The observed anisotropy is then interpreted by assuming that the microfracture behaviour is correlated principally to the presence of slip planes. The role of slip planes correctly oriented with respect to the specimen surface and to the direction of scratching has been easily recognized on scanning electron micrographs of scratches. The main results summarized in Table X show, without ambiguity, that all the slip planes contribute to chipping.

References

1. J. R. WIG, J. W. LEBUS and R. FILLER, Report ECOM-4548, US Army Research and Development Command, Fort Monmouth, NJ (1977).
2. P. VIGOUREUX and C. F. BOOTH, "Quartz Vibrators and their Applications" (HMSO, London, 1950) Ch. 5.
3. C. R. TELLIER and J. L. VATERKOWSKI, *Surf. Technol.* **26** (1985) 275.
4. Y. SEKIGUCHI and H. FUNAKUBO, *J. Mater. Sci.* **15** (1980) 3066.
5. F. FUKUYO, N. OURA, N. KITAJIMA and H. KONO, *J. Appl. Phys.* **50** (1979) 3653.
6. B. LAMY, Thesis, Université de Haute-Alsace, France, August 1982.
7. J. BIASOLI DE MELLO, Thesis, Institut National Polytechnique de Grenoble, France, October 1983.
8. M. A. MOORE, *Wear* **27** (1974) 1.
9. M. C. SHAW, "Fundamentals of Grinding, New Developments in Grinding" (Carnegie Press, Pittsburgh, PA, 1972).
10. B. R. LAWN, *Proc. R. Soc. Lond.* **A299** (1967) 307.
11. B. R. LAWN and T. R. WILSHAW, *J. Mater. Sci.* **10** (1975) 1049.
12. N. MAAN and A. BROESE VAN GROENOU, *Wear* **42** (1977) 365.
13. B. R. LAWN, *J. Appl. Phys.* **39** (1968) 4228.
14. F. B. LANGITAN and B. R. LAWN, *ibid.* **10** (1969) 4009.
15. B. R. LAWN and A. G. EVANS, *J. Mater. Sci.* **12** (1977) 2195.
16. F. C. FRANK and B. R. LAWN, *Proc. R. Soc. Lond.* **A299** (1967) 291.
17. N. E. W. HARTLEY and T. R. WILSHAW, *J. Mater. Sci.* **8** (1973) 265.
18. W. F. BRACE, *J. Geol.* **71** (1963) 581.
19. C. A. BROOKES, J. B. O'NEILL and B. A. W. REDFERN, *Proc. R. Soc. Lond.* **A322** (1971) 73.
20. B. R. LAWN and M. V. SWAIN, *J. Mater. Sci.* **10** (1975) 113.
21. T. G. MATHIA, M. BARQUINS, *Ind. Ceram.* **791** (1985) 111.
22. IEEE Standard on Piezoelectricity (IEEE, New York, 1978).
23. B. R. LAWN and D. B. MARSHALL, *J. Am. Ceram. Soc.* **62** (1979) 347.

24. P. CASTET and C. GONIN, Internal Report, Ecole Nationale Supérieure de Mécanique et des Microtechniques, Besançon, France, June 1991.
25. C. TELLIER and A. RASLAN, Internal Report, Laboratoire de Chronométrie, Electronique et Piézoélectricité, Ecole Nationale Supérieure de Mécanique et des Microtechniques, Besançon, France, October 1991.
26. W. G. CADY, "Piezoelectricity", Vol. 2 (Dover, New York, 1964).

Received 18 January
and accepted 3 February 1993